Contrib. Astron. Obs. Skalnaté Pleso **43**, 5 – 26, (2013)

Search for Alfvén waves in a bright network element observed in Hα

J. Koza[1], P. Sütterlin[2], P. Gömöry[1], J. Rybák[1] and A. Kučera[1]

[1] *Astronomical Institute of the Slovak Academy of Sciences 059 60 Tatranská Lomnica, The Slovak Republic, (E-mail: koza@astro.sk)*

[2] *Institute for Solar Physics, The Royal Swedish Academy of Sciences, Alba Nova University Center, 106 91 Stockholm, Sweden*

Received: January 28, 2013; Accepted: February 20, 2013

Abstract. Alfvén waves are considered as potential transporters of energy heating the solar corona. We seek spectroscopic signatures of the Alfvén waves in the chromosphere occupied by a bright network element, investigating temporal variations of the spectral width, intensity, Dopplershift, and the asymmetry of the core of the Hα spectral line observed by the tunable Lyot filter installed on the Dutch Open Telescope. The spectral characteristics are derived through the fitting of five intensity samples, separated from each other by 0.35 Å, by a 4$^{\rm th}$-order polynomial. The bright network element displays the most pronounced variations of the Dopplershift varying from 0 to 4 km s^{-1} about the average of 1.5 km s^{-1}. This fact implies a persistent redshift of the Hα core with a redward asymmetry of about 0.5 km s^{-1}, suggesting an inverse-C bisector. The variations of the core intensity up to $\pm$10 % and the core width up to $\pm$5 % about the respective averages are much less pronounced, but still detectable. The core intensity variations lag behind the Dopplershift variations about 2.1 min. The Hα core width tends to correlate with the Dopplershift and anticorrelate with the asymmetry, suggesting that more redshifted Hα profiles are wider and the broadening of the Hα core is accompanied with a change of the core asymmetry from redward to blueward. We also found a striking anticorrelation between the core asymmetry and the Dopplershift, suggesting a change of the core asymmetry from redward to blueward with an increasing redshift of the Hα core. The data and the applied analysis do not show meaningful tracks of Alfvén waves in the selected network element.

Key words: Sun: chromosphere – Line: profiles

1. Introduction

Alfvén waves have been invoked as one of possible mechanisms heating the solar corona (Alfvén, 1947; Osterbrock, 1961). These magnetic transporters of convective energy are capable of penetrating through the solar atmosphere without being reflected and refracted. Since Alfvén waves are incompressible, their propagation through the atmosphere is not associated with density changes seen as periodic variations of intensities and line-of-sight velocities (Erdélyi & Fedun, 2007; Mathioudakis *et al.*, 2012). Observation of a slanted magnetic fluxtube could reveal Alfvén waves as periodic variations of nonthermal broadening of a spectral line. This approach was employed in the study by Jess *et al.* (2009) who found periodic oscillations of nonthermal broadening of the Hα spectral line seen over a cluster of bright points associated with a distinct upflow without significant periodic variations of intensities and line-of-sight velocities. They interpret this as a manifestation of Alfvén waves in the solar atmosphere. However, there is some ambiguity whether they deal with spectral or integrated intensities.

Motivated by the results of Jess *et al.* (2009), we search for signatures of Alfvén waves in a bright network element occupied by a cluster of G-band bright points. We investigate spectral characteristics of the Hα spectral line, focusing on temporal variations of the line core width, intensity, Dopplershift, and the asymmetry derived by a 4$^{\mathrm{th}}$-order-polynomial fitting of a coarse five-point sampling of the Hα profile. Since we employ the correcting method and results of Koza *et al.* (2013), and frequently refer to it as Paper I hereafter, we invite the reader to have it handy.

2. Observations

We use sequences of Hα images of a very quiet area near the disk center ($\mu =$ 0.91) recorded by the Dutch Open Telescope (DOT) on 19 October 2005 from 09:55:20 UT to 11:05:47 UT by the tunable Lyot filter with a *FWHM* passband of 0.25 Å (Gaizauskas, 1976; Bettonvil *et al.*, 2006). The sequence consists of scans taken in five wavelengths across the Hα line profile: line center, $\pm$0.35 Å and $\pm$0.7 Å, followed by a single image in the line center. The zero wavelength of the filtergrams is centered on the minimum of an average profile taken before the observations over the field of view. A time step between the five-wavelength scans of the Hα line profile and line center images is 30 s. Since the images at two subsequent wavelengths are separated by the 4-to-5-s intervals, one full 5-point scan of the Hα profile took about 20-25 s. Within this interval no major changes of chromospheric scenery are assumed. The scans were taken in 20-frame bursts per particular wavelength setting and then speckle-reconstructed applying a Keller - von der Lühe two-channel reconstruction (Keller & von der Lühe, 1992). The line center images were obtained in 100-frame bursts restored by a full single-channel speckle reconstruction. In this study, we employ 71 Hα scans at a regular 60-s cadence taken between 09:55:20 UT and 11:05:22 UT. The seeing was only fair, with the Fried parameter r_0 slightly increasing from about 7.5 at the beginning to 9 on average at the end of the observation. As a context data, we also use the sequences of 142 G-band and Ca II H images taken synchronously with the Hα images at a regular 30-s cadence. The temporal mean of the Ca II H images and examples of the Hα images taken during the period of the best seeing are shown in Figs. 1–3. The size of the Ca II H and Hα images is $1112 \times 818\,\mathrm{px}^2$, with the angular size of pixel of 0.071 arcsec. Details on the DOT, its tomographic multiwavelength imaging, speckle reconstruction, and

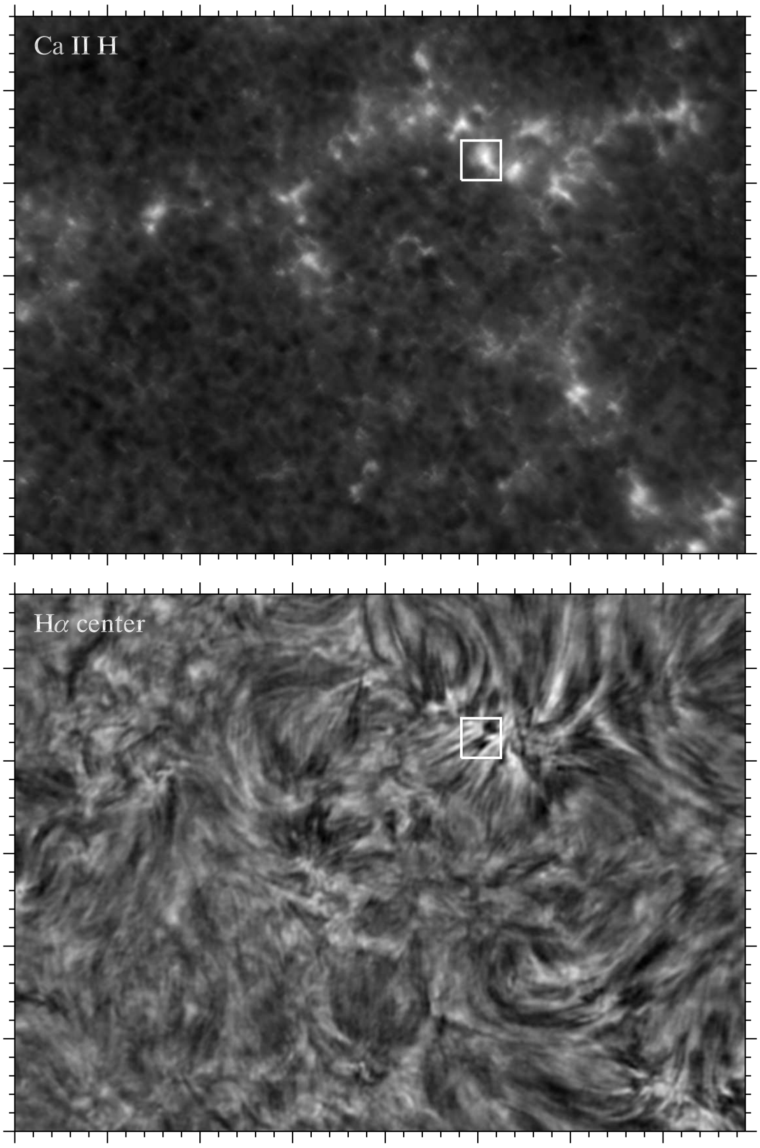

Figure 1. Images of the quiet-Sun network recorded by DOT on 19 October 2005. *Top:* the temporal mean of the Ca II H image sequence over its 71-min duration. *Bottom:* the Hα image taken at 10:36:21 UT in the line center at the moment of the best seeing occurred in the 41$^{\mathrm{st}}$ min after the start of the observation at 09:55:20 UT. The square defines the network element selected for this study and displayed in detail in Figs. 4–7. Field of view: 79 × 58 arcsec^2. Tickmark spacing: 2 arcsec.

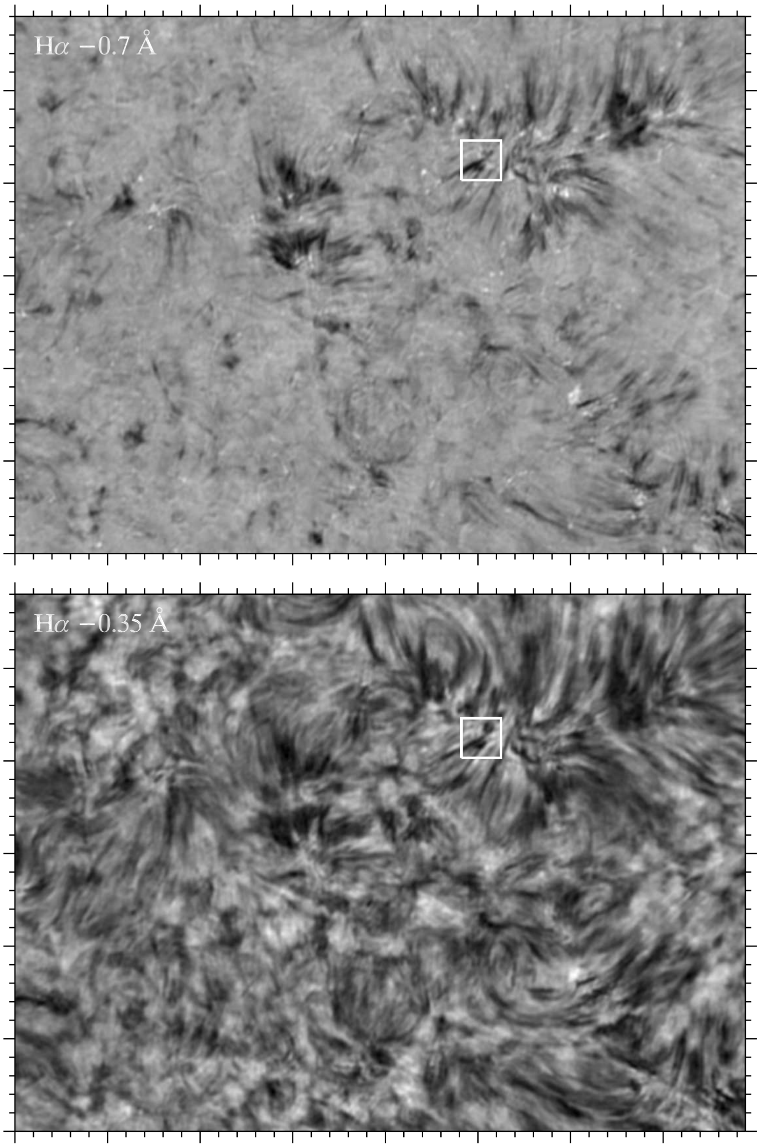

Figure 2. DOT Hα images at $\Delta\lambda = -0.7$ Å (*top*) and -0.35 Å (*bottom*) from the line center corresponding to the Hα line-center image in Fig. 1.

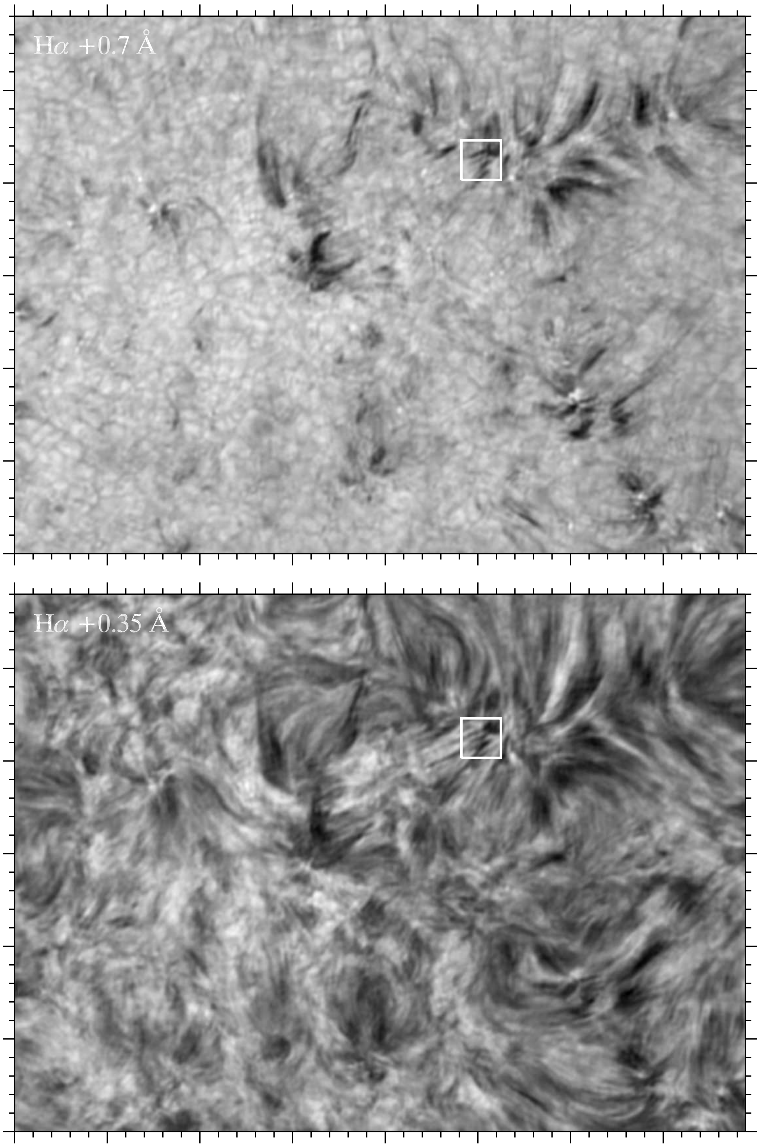

Figure 3. DOT Hα images at $\Delta\lambda = +0.7$ Å (*top*) and $+0.35$ Å (*bottom*) from the line center corresponding to the Hα images in Figs. 1 and 2.

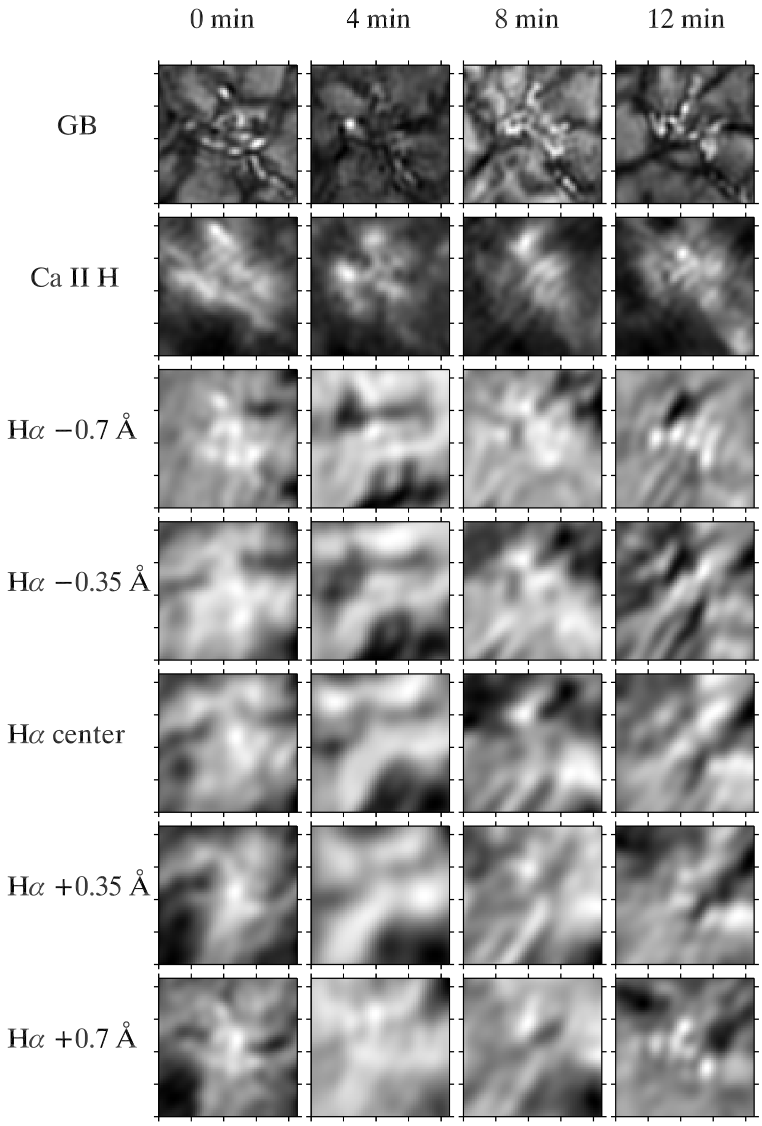

Figure 4. Temporal evolution of the selected network element seen simultaneously in the DOT G-band, Ca II H, and Hα images taken at five wavelength settings of the Hα Lyot filter. The time 0 min corresponds to the moment of the start of the observation at 09:55:20 UT. Field of view: $4.3 \times 4.3\,\mathrm{arcsec}^2$. Tickmark spacing: 1 arcsec.

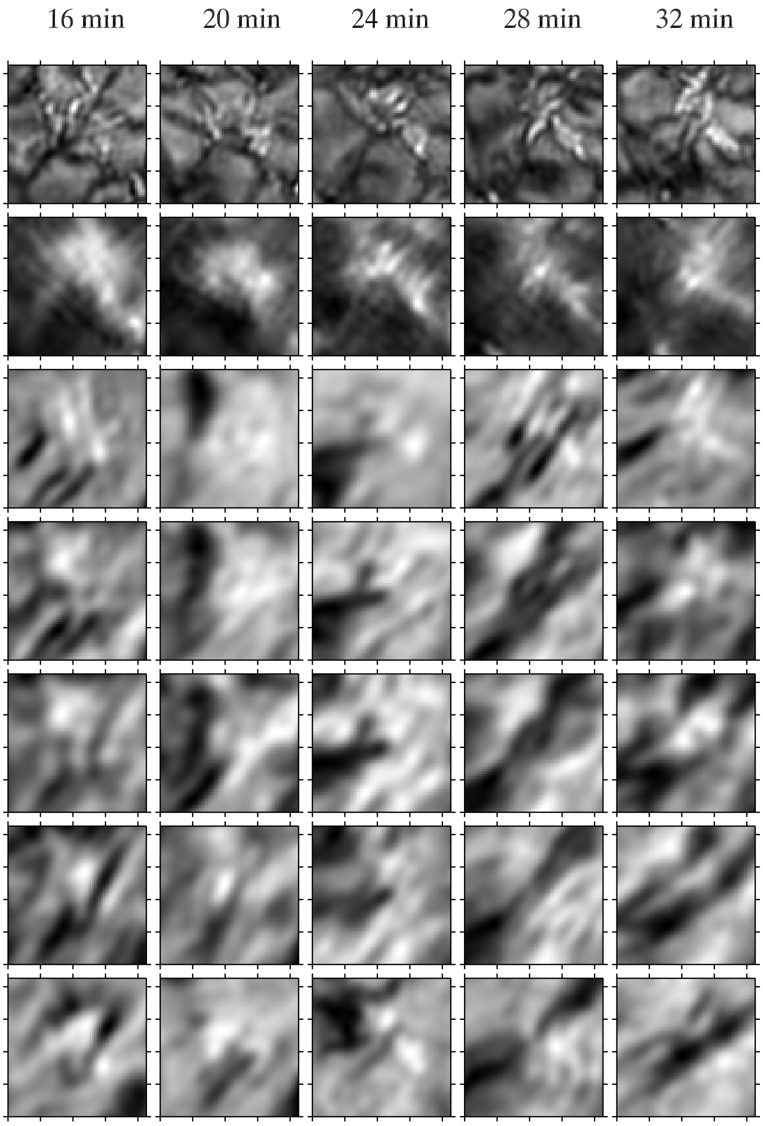

Figure 5. The same as in Fig. 4.

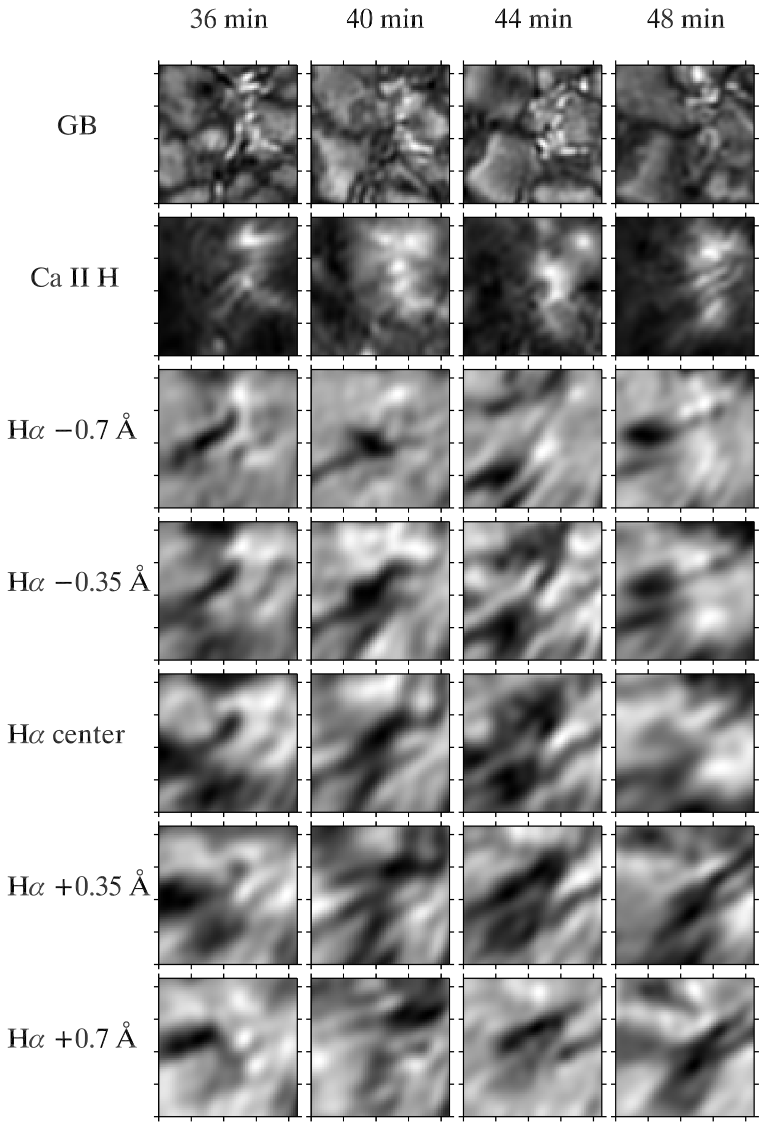

Figure 6. The same as in Fig. 4.

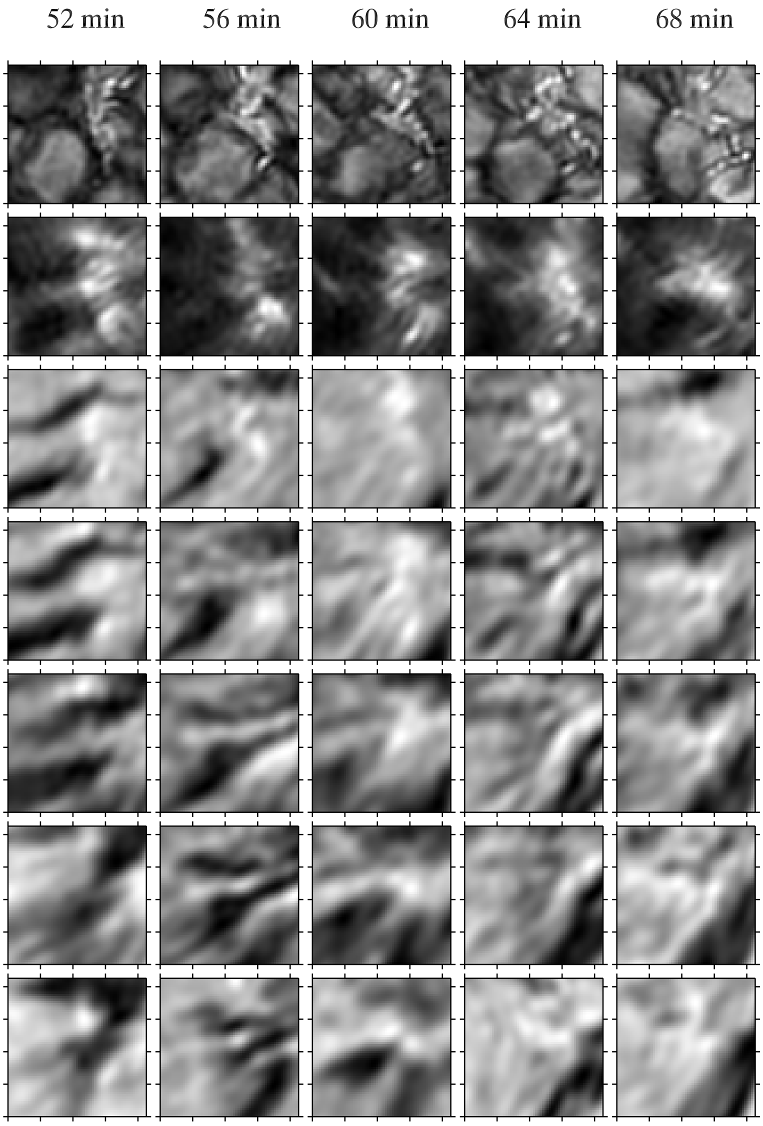

Figure 7. The same as in Fig. 4.

standard reduction procedures are given in Hammerschlag & Bettonvil (1998) and Rutten *et al.* (2004).

The target area encompasses a full supergranular cell surrounded by a prominent network as seen in the temporal mean of the Ca II H sequence in Fig. 1. Visual comparison of both panels in Fig. 1 indicates that the brightest network elements coincide with roots of long chromospheric fibrils. These dominate Hα scene and emanate out from the network elements outlining the structure of magnetic field at chromospheric levels. DOT Hα scans render a tomographic view of the solar atmosphere from the photosphere (Figs. 2 and 3: ± 0.7 Å) up to the chromosphere sampled by the images in the line center and ± 0.35 Å off (Kontogiannis *et al.*, 2010). In the Hα $+0.7$ Å image (Fig. 3, top), we can clearly see granulation which is missing in the Hα -0.7 Å image (Fig. 2, top) due to Doppler cancellation. Both images display dark elongated streaks which are highly-dopplershifted parts of fibrils seen better in the line center and ± 0.35 Å images. Doppler cancellation enhances the visibility of magnetic elements seen as bright points in the Hα -0.7 Å image (Fig. 2, top), studied in detail in Leenaarts *et al.* (2006). The square defines the network element selected for this study. The size of the square is $61 \times 61\,\mathrm{px}^2$, corresponding to $4.3 \times 4.3\,\mathrm{arcsec}^2$.

Figs. 4–7 show enlargements of the square providing a multispectral tomographic view on evolution of the selected network element unfolded in time with a 4-min timestep from the lower photosphere (G band) up to the chromosphere (Hα line center). The G-band cutouts show a cluster of bright points constituting the network element. The selected area also involves two large granules, with maximum diameters larger than 2 arcsec, occurring in the lower half from 16 to 28 min (Fig. 5) and from 44 to 68 min (Figs. 6 and 7). The Ca II H cutouts show brightenings whose overall morphology is often very similar to that of the cluster of the G-band bright points. But the former are strongly diffuse because of resonance scattering within the solar atmosphere and through expansion of idealized magnetostatic fluxtubes with height (Leenaarts *et al.*, 2006). The Hα outer wing cutouts (± 0.7 Å) mix photospheric and chromospheric features because of a double-peak contribution function at Hα wings (Schoolman, 1972; Leenaarts *et al.*, 2006, 2012). Striking, almost one-to-one correspondence between the G-band bright points and the blue wing bright points seen in -0.7 Å (compare the G-band and Hα -0.7 Å cutouts, *e.g.*, at 0, 12, 32, 60, and 64 min) was explained in Leenaarts *et al.* (2006). The line center and ± 0.35 Å cutouts bear still signatures of a network brightening, but modulated much with a fast-changing blanket of the dark fibrils occurring higher up.

3. Method, spectral characteristics, and their corrections

The coarse five-point sampling enables us to construct $1112 \times 818 \times 71$ instantaneous proxy profiles of the Hα spectral line at each pixel. We fit the five-wavelength samples of the proxy profiles by a 4^{th}-order polynomial to derive the four basic profile measurements: the core intensity I_{C}, the core velocity v_{C}, the core width FW, and the bisector velocity v_{BI}. The values of I_{C} and v_{C} represent the fit minimum and its Dopplershift, respectively. The core width is the wavelength separation of the two fit flanks at half of the intensity range between the fit minimum and the average of the endpoint intensities at ± 0.7 Å. The core width is computed at the average intensity I_{FW} employing the reference intensity I_{RF1} defined by equations (3) and (4) in Paper I. Finally, the bisector velocity is the velocity equivalent of the wavelength separation between the midpoint of the fit at the average intensity I_{FW} and the fit minimum. A more detailed definition of the spectral characteristics is given in Paper I. In case of a large Dopplershift, when the average intensity is larger than the minimum of endpoint intensities, *i.e.*, $I_{\mathrm{FW}} > \min(I_{-0.7}, I_{+0.7})$, the fits are extrapolated beyond the range ± 0.7 Å using the polynomial coefficients and the extrapolated fits are used for determining the spectral characteristics. In very rare cases of a polynomial undulation, with local maxima lower than the average intensity I_{FW}, the algorithm switches to a parabolic fit of the five-point proxy profile to determine FW, while I_{C} and v_{C} are always from the 4^{th}-order-polynomial fit and v_{BI} is undefined. The extrapolation (Fig. 8) was invoked just in 0.024 % and the parabolic fit in 5×10^{-4} % out of all pixels. The intensities shown in Figs. 8 and 9 were normalized with respect to the mean intensities resulting from spatio-temporal averaging of the respective image cubes. The five mean intensities were converted to the atlas intensity scale convolving the Hα atlas profile with the transmission profile of the DOT Hα filter (Paper I, equation (1)). Therefore, the integrated intensities in Figs. 8 and 9 are in the wavelength unit.

The five intensity samples have an instrumental wavelength scale ranging from -0.7 to 0.7 Å. The wavelengths of particular core fit minima λ_{C} are measured with respect to this instrumental wavelength scale with milliångström resolution and then converted to the core velocity as: $v_{\mathrm{C}} = c(\lambda_{\mathrm{C}} - \lambda_{\mathrm{R}})/\lambda_0$, where c is the speed of light, λ_0 is the central wavelength of the Hα line 6562.8 Å, and the reference wavelength λ_{R} is the spatio-temporal average of all $1112 \times 818 \times 71$ wavelengths of fit minima λ_{C} over all pixels within the field of view, making no distinction between network and internetwork pixels. The reference wavelength λ_{R} is about -18 mÅ. An adopted sign convention indicates a redshift of the line core fit for positive Dopplershift and v_{C}. The bisector velocity v_{BI} quantifies an asymmetry of the line core fit with respect to its minimum. The sign convention adopted in Paper I suggests positive v_{BI} for a line core fit with a redward asymmetry.

To eliminate the modulation of the spectral characteristics induced by the fast-changing blanket of dark fibrils, we construct 71 proxy Hα profiles by spatial averaging of intensities within the selected network element (Figs. 4–7) at each wavelength. Fig. 9 shows examples of these spatially averaged intensities, their polynomial fits, average intensities, and core velocities. Spectral characteristics of these spatially averaged intensities are determined solely from their 4^{th}-order-polynomial non-extrapolated fits. To asses an influence of the averaging on the

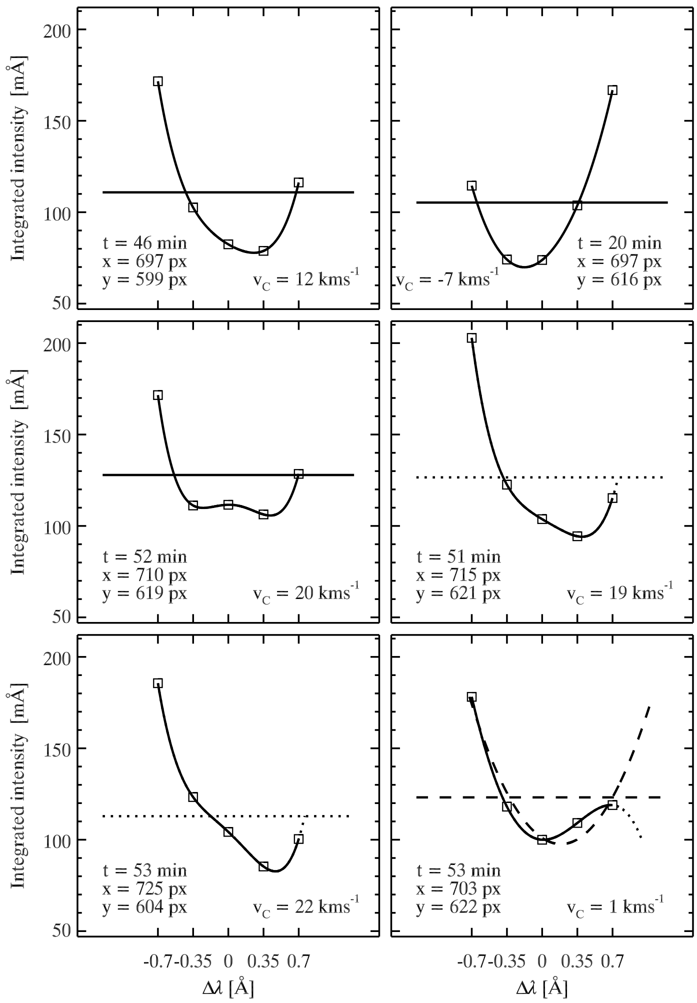

Figure 8. Examples of observed intensities (squares), their $4^{\rm th}$-order-polynomial (solid), extrapolated (dotted), and parabolic (dashed) fits taken from various locations x, y over the selected network element at the indicated time t. The horizontal lines indicate the average intensity defining the fit width and the bisector velocity. Their solid, dotted, and dashed linestyles correspond to the $4^{\rm th}$-order-polynomial, extrapolated, and parabolic fits, respectively, used in determination of the fit width and the bisector velocity. The coordinates x, y refer to the lower left corners of images. The selected samples do not represent majority, but rather rare cases with a high core velocity $v_{\rm C}$ and highly asymmetric profiles (the middle and bottom panels).

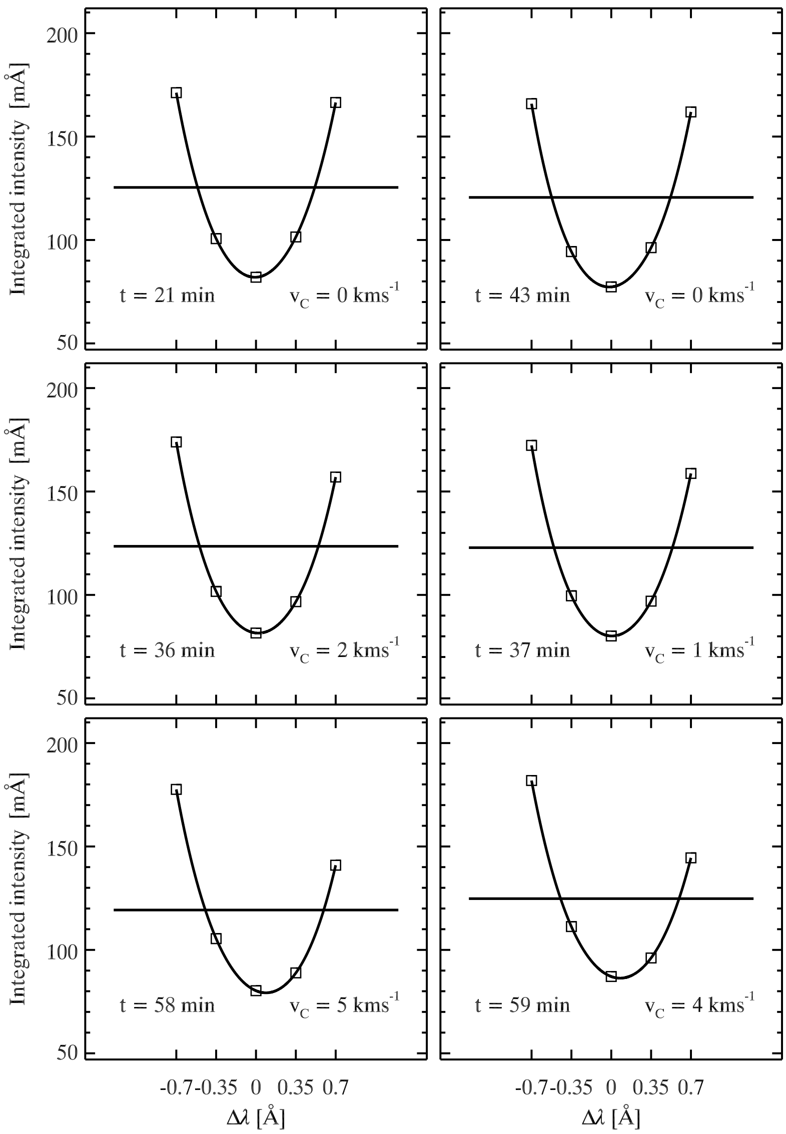

Figure 9. Examples of observed intensities (squares) averaged over the selected network element (Figs. 4–7) and their 4$^{\mathrm{th}}$-order-polynomial fits (solid) at the given time t. The horizontal lines indicate the average intensity defining the fit width and the bisector velocity. The samples illustrate the fits with small (top), medium (middle), and high (bottom) redshift with the core velocity v_{C}.

final results, we compare them with the instantaneous characteristics obtained by the spatial averaging of FW, $I_{\rm C}$, $v_{\rm C}$, and $v_{\rm BI}$ within the selected area (Figs. 4–7). Both, the instantaneous spectral characteristics inferred per pixel and also from the spatially averaged intensities are corrected for the deviations estimated in Paper I comparing the measurements of FW, $I_{\rm C}$, $v_{\rm C}$, and $v_{\rm BI}$ performed at the dopplershifted Hα atlas profile convolved with the filter transmission with their reference values. Then the corrected core velocity $v_{\rm C}$ is the solution of the equation $f(v_{\rm C}) + v_{\rm C} - \nu = 0$, where $f(v_{\rm C})$ is the absolute deviation Δv and ν is the measured core velocity. The corrected FW results from the equation $FW = fw - \Delta FW(v_{\rm C})$, where fw is the measured fit width and $\Delta FW(v_{\rm C})$ is the absolute deviation ΔFW, but interpolated on the corrected core velocity $v_{\rm C}$. The corrected $v_{\rm BI}$ is computed in the same way. Due to different intensity scales, the corrected $I_{\rm C}$ results from the equation $I_{\rm C} = i/(1 + \Delta I_{\rm r}(v_{\rm C})/100)$, where i is the measured core intensity and $\Delta I_{\rm r}(v_{\rm C})$ is the relative deviation $\Delta I_{\rm r}$, but interpolated on the corrected core velocity $v_{\rm C}$.

4. Noise, data uncertainties, and references

Reliability of results inferred by fitting depends critically on the noise presented in the data and various intrinsic uncertainties. Therefore, in this section we give a brief account of uncertainties of the fitted intensities and the reference wavelength defining the core velocity.

We estimated the upper limit of the noise level $1\sigma_{\rm NOISE}$ presented in the Hα filtergrams from 1σ of the temporal variations of the intensity at each pixel assuming that $1\sigma_{\rm NOISE} \leq 1\sigma/10$. In other words, we assumed that the noise level is about one order smaller than 1σ of the temporal variations of the intensity due to physical processes on the Sun within the 71-min observing period. This rough estimate points out that these $1\sigma_{\rm NOISE}$ errors of the intensities in Fig. 8 are smaller than the height of the square symbols and can therefore be neglected.

Similarly, we estimated the noise level of the spatially-averaged intensities in Fig. 9 from 1σ of the spatial variations of the intensity over the selected area. In other words, we assumed that the per-pixel noise level within the area is 1σ of intensity variations over the area. However, the spatial averaging of the intensities reduces their noise level by a factor of $1/\sqrt{N}$ or 1/61, where N is the number of averaged pixels. This again points out, that the errors of intensities in Fig. 9 are much smaller than the height of the square symbols and are thus insignificant.

In this paper, we define the reference wavelength $\lambda_{\rm R}$, or zero point of the core velocity, as the spatio-temporal average of the wavelengths $\lambda_{\rm C}$ of the core fit minima determined at each pixel. We estimated uncertainty or stability of $\lambda_{\rm R}$ during the 71-min observing period in two ways. First, we constructed 71 proxy Hα profiles from instantaneous spatially-averaged intensities, determined the wavelengths of their core fit minima, and computed the median of their absolute differences from the total average. Second, we took 71 spatial averages of the wavelengths of core fit minima for each moment of the observation and computed again the median of their absolute differences from the total average. Both estimates gave consistent results, indicating that uncertainty of the reference wavelength λ_R of the core velocity is about $\pm 0.3\,\mathrm{km\,s^{-1}}$.

When determining the reference wavelength λ_R we made no distinction between the network and internetwork areas and this might be a source of a systematic offset. We checked this feature by selecting only large internetwork areas for determination of λ_R. This one is blueshifted about $0.2\,\mathrm{km\,s^{-1}}$ with respect to the reference wavelength from the whole field of view.

5. Results

This section presents a pictorial overview of results inferred from the data undergone various processing. Gray shades in Figs. 10 – 12 highlight differences between the uncorrected (gray) and corrected (black) data, while the different styles distinguish the results of intensity averaging (solid lines) and spatial averaging of spectral characteristics (symbols) over the network element.

5.1. Temporal evolution of the spectral characteristics

The top panel of Fig. 10 shows temporal evolutions of the relative variations of the fit width FW and the core intensity I_C of the line core fits of the Hα spectral line in the network element (Figs. 4–7) with respect to their temporal means. The bottom panel shows temporal evolutions of the core velocity v_C and the bisector velocity v_BI, whose positive values indicate redshift and redward asymmetry of the line core. All these characteristics were derived from the original Hα datacubes downloaded from the DOT database[1]. An application of the corrections (Paper I) increases apparently the amplitude of the FW variations after the 40^th min, but decreases both velocities within the whole 71-min period. The values of FW and I_C seem to be largely insensitive to the choice of averaging for the size of the selected area, but this is not the case of v_C and v_BI. Their corrected values resulting from spatial averaging over the network element (black diamonds and triangles in the bottom panel) differ systematically from the values inferred from spatial means of the intensities (black thick and thin lines). This is probably due to high non-linearity of the respective correcting functions shown in Paper I. The temporal evolutions of the characteristics do not show any apparent systematic trend and fast short-period variations dominate them. The variations of corrected FW are within the range $\pm 5\,\%$ around the mean. The variations of I_C indicate a rapid darkening of the selected network element (Fig. 4) from 11 % above an average to average within the first 10 minutes. Later on, I_C variations lie within the range from $-9\,\%$ to $+6\,\%$. The

[1] `http://dotdb.strw.leidenuniv.nl/DOT/`

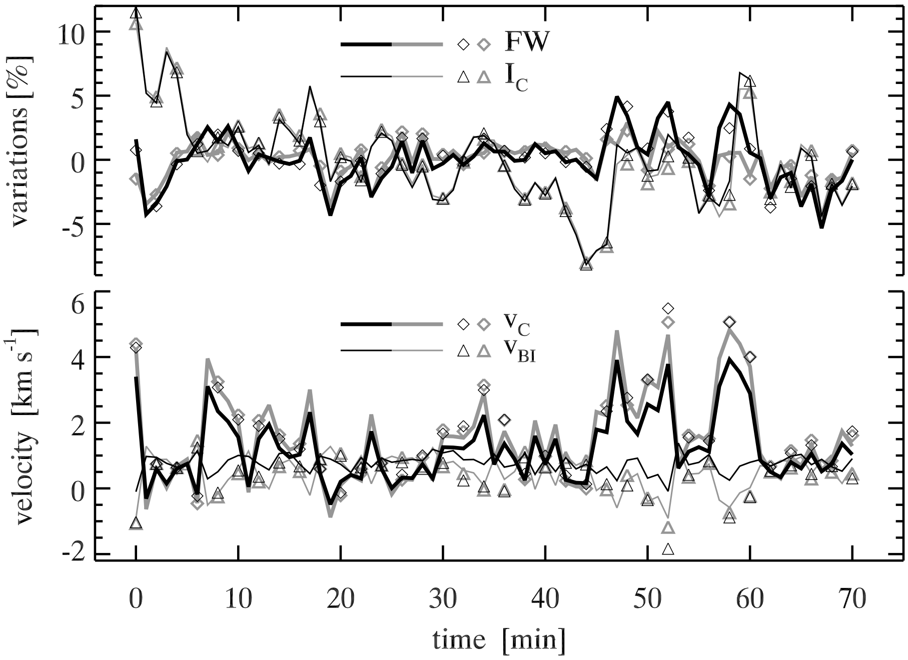

Figure 10. Temporal evolution of the fit width *FW*, the core intensity $I_{\rm C}$, the core velocity $v_{\rm C}$, and the bisector velocity $v_{\rm BI}$ of the line core fit of the Hα spectral line in the network element (Figs. 4–7) derived by the 4$^{\rm th}$-order polynomial. *FW* and $I_{\rm C}$ are shown as variations with respect to their temporal means (top panel). Positive $v_{\rm C}$ and $v_{\rm BI}$ signalize a redshift (middle and bottom panel). Gray and black lines indicate the uncorrected and corrected characteristics, respectively, derived from spatial means of the intensities. Gray and black symbols shown with the time step of 2 min indicate the uncorrected and corrected characteristics, respectively, derived as spatial means of particular values at each pixel.

corrected $v_{\rm C}$ displays redshifts up to 4 km s^{-1}, with an average of 1.5 km s^{-1} and a noticeable correlation with the corrected *FW*, most apparent after the fortieth minute. In the same period, a large expanding granule with the maximum diameter larger than 2 arcsec appeared in the low photosphere (see Figs. 6 and 7). Fig. 10 suggests also some similarity between the $v_{\rm C}$ and $I_{\rm C}$ variations. The Fourier cross correlation indicates that $I_{\rm C}$ lags behind $v_{\rm C}$ about 2.1 min on average. The Hα core possesses mostly a redward asymmetry corresponding to an inverse-C bisector with the average bisector velocity of about 0.5 km s^{-1} with excursions up to 1 km s^{-1}.

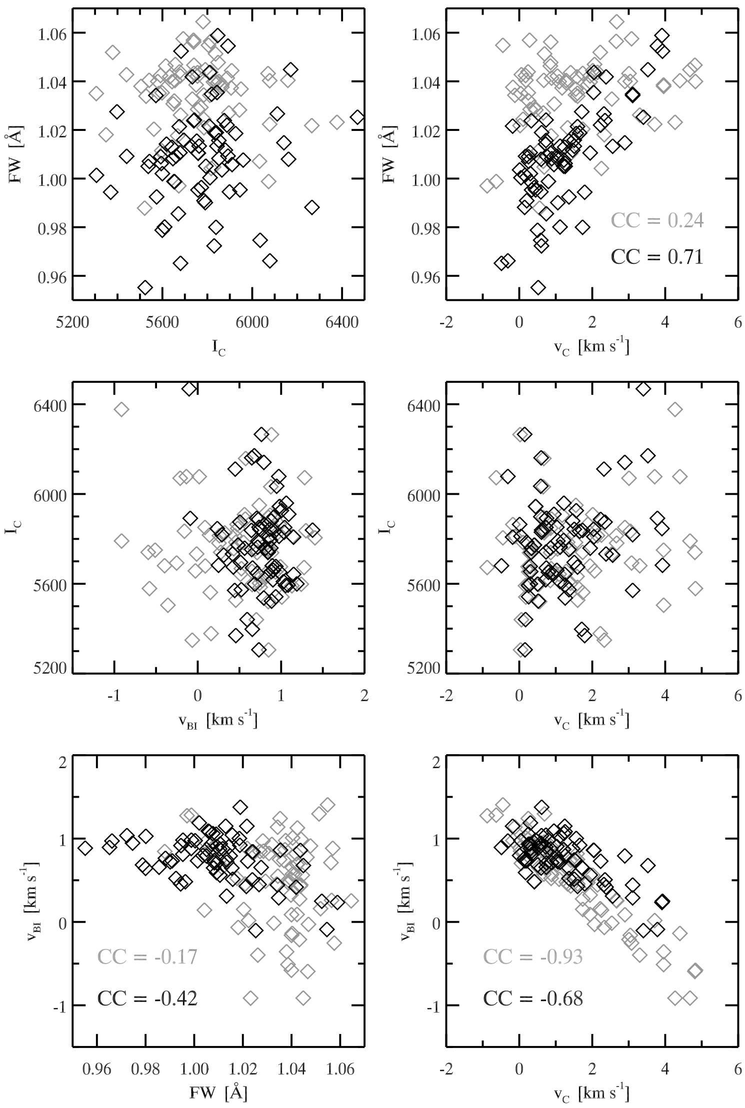

Figure 11. Scatter plots of the spectral characteristics shown in Fig. 10 – the case of spatial means of the intensities. Gray and black symbols indicate the uncorrected and corrected characteristics, respectively. Unlike Fig. 10, the plots show absolute values of FW and I_C. Positive v_C and v_{BI} signalize a redshift. There are also shown the correlation coefficients CC for the pairs $FW - v_C$, $v_{BI} - FW$, and $v_{BI} - v_C$ for uncorrected (gray) and the corrected (black) values.

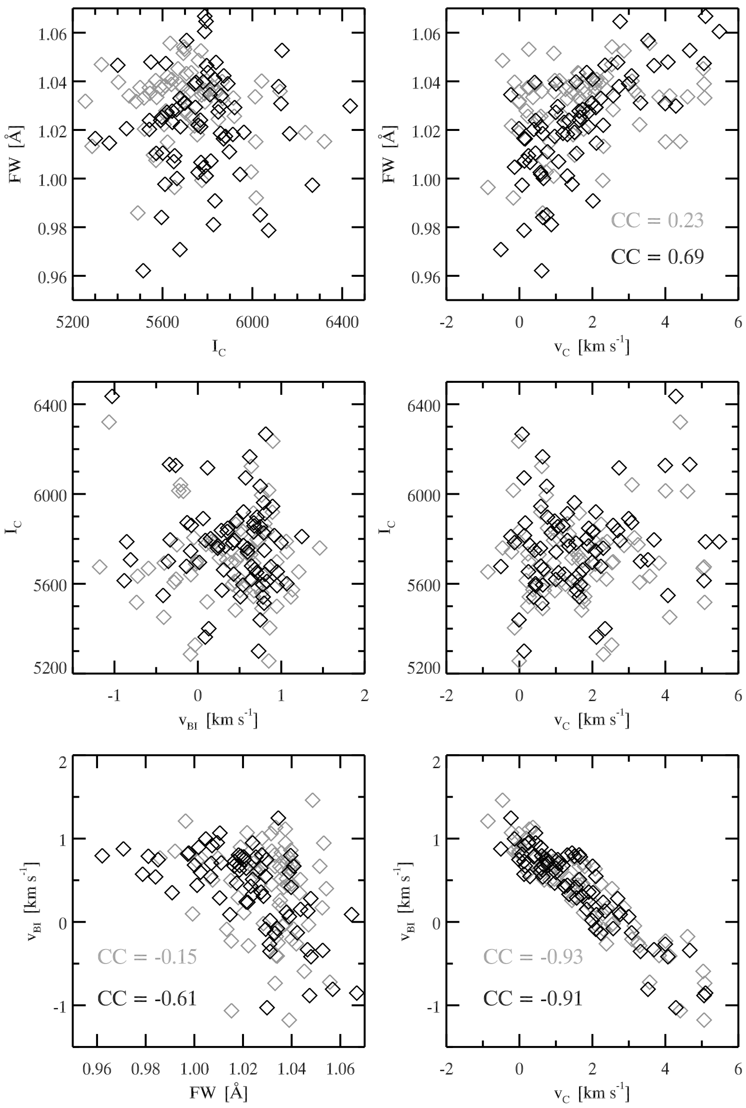

Figure 12. Scatter plots of the spectral characteristics shown in Fig. 10 – the case of spatial means of the spectral characteristics at each pixel. Gray and black symbols indicate the uncorrected and corrected characteristics, respectively. Unlike Fig. 10, the plots show absolute values of FW and $I_{\rm C}$. Positive $v_{\rm C}$ and $v_{\rm BI}$ signalize a redshift. There are also shown the correlation coefficients CC for the pairs $FW - v_{\rm C}$, $v_{\rm BI} - FW$, and $v_{\rm BI} - v_{\rm C}$ for the uncorrected (gray) and corrected (black) values.

5.2. Scatter plots

The spectral characteristics from Fig. 10 are displayed in the form of scatter plots in Figs. 11 and 12, showing separately the results of spatial averaging of the intensities and the spectral characteristics at each pixel, respectively. The top left panels show FW against I_{C} which do not correlate, neither uncorrected nor corrected. The top right panels suggest a positive correlation between FW and v_{C}, which occurs only for the corrected values. The correlation implies that more redshifted profiles tend to be wider. The middle panels indicate that there is no apparent correspondence between I_{C} and the velocities. The values of I_{C} do not correlate with v_{C}, not even after shifting I_{C} forward (*i.e.*, to the left with respect to the zero of the time axis) about 2.1 min to compensate its apparent lag indicated in Fig. 10. The bottom left panel of Fig. 12 suggests an anticorrelation between v_{BI} and FW, which occurs only for the corrected values resulting from their spatial averaging at each pixel. The anticorrelation implies that while narrower Hα cores display a redward asymmetry, the wider and more redshifted profiles (see the $FW - v_{\mathrm{C}}$ correlation above) display a blueward asymmetry. The bottom right panels also suggest a striking anticorrelation between v_{BI} and v_{C}. Notably, the profiles with the zero Dopplershift display a redward asymmetry with $v_{\mathrm{BI}} = 1\,\mathrm{km\,s^{-1}}$ and become symmetric for v_{C} of $2\,\mathrm{km\,s^{-1}}$, but tend to display an increasing blueward asymmetry with further-increasing redshift.

6. Discussion

We derived spectral characteristics of the Hα spectral line observed in the network element with the aim of seeking signatures of the Alfvén waves as reported in Jess *et al.* (2009). How do our findings compare to the results of these authors? While Jess *et al.* (2009) reported an average blueshift of $23\,\mathrm{km\,s^{-1}}$ in a cluster of bright points seen in Hα, we found an average redshift of about $1.5\,\mathrm{km\,s^{-1}}$. Obviously, this is a large discrepancy and we suspect that our particular choice of the reference wavelength of the core velocity might be partially responsible for that. We remind that we made no distinction between the network and internetwork (see Section 3). But as we showed in Section 4, selecting only internetwork areas shifts the reference wavelength blueward only insignificantly up to $0.2\,\mathrm{km\,s^{-1}}$ and the value of the average redshift is significantly above the uncertainty of $0.3\,\mathrm{km\,s^{-1}}$ of the reference wavelength. Further, Jess *et al.* (2009) reported an absence of any significant intensity variations in the cluster of bright points. However, there is some uncertainty whether they refer to the spectral intensity in the line core, or the integrated intensity. Our results suggest that the core width variations in the selected network element are associated with both the core velocity and core intensity variations. Finally, the authors detected $FWHM$ oscillations of the Hα spectral line with the strongest power in the 400-to-500 s interval. We postpone detailed cross correlation, Fourier, and wavelet analyzes of our results to a forthcoming paper. We conclude that, most likely, a different mechanism works in the selected network element than in the cluster of the bright points studied by Jess *et al.* (2009). The inverse-C bisector and the average redshift of the Hα line core are more symptomatic for propagation of chromospheric shocks, as suggested in Uitenbroek (2006) and demonstrated in numerical simulations by Heggland *et al.* (2011). Then the lagging of the core intensity $I_{\rm C}$ behind the core velocity $v_{\rm C}$ variations about 2.1 min might be characteristic either for the p-mode oscillations leaking into the chromosphere, or for the shock wave propagation. Although there is an apparent similarity of their variations best seen after the fortieth minute (Fig. 10), shifting $I_{\rm C}$ forward about the 2-min lag does not improve the $I_{\rm C} - v_{\rm C}$ correlations shown in the middle right panels of the scatter plots in Figs. 11 and 12, which may be ascribed to a variable phase shift which varies in time and/or frequency.

Since the standard DOT observations do not involve any precise wavelength calibration of the Hα filtergrams, we refrained from interpreting straightforwardly redshifts and blueshifts as actual mass downflows and upflows, respectively. Despite these facts, we will try to reason that most of the positive values of $v_{\rm C}$ indicated by the redshifts of the Hα core may represent the actual mass downflows. As we noted in Section 2, the zero wavelength of the filtergrams is centered on the minimum of an average profile taken before the observations over the field of view. Thus, the zero wavelength approximately corresponds to the Hα solar disc-center wavelength of $\lambda_{\rm sol} = 6562.81$ Å according to the spectral FTS atlas by Neckel (1999), whose wavelength scale was already corrected for the rotational and radial velocity of the Earth. Consequently, the reference wavelength given in Section 3 corresponds to $\lambda_{\rm R} = \lambda_{\rm sol} - 0.018$ Å $=$ 6562.79 Å. The local standard of rest at the solar surface for the Hα spectral line is: $\lambda_0 = \lambda_{\rm lab}(1 + v_{\rm GR}/c) = 6562.80$ Å, where $\lambda_{\rm lab} = 6562.79$ Å is the air laboratory wavelength of Hα adopted from the NIST database (Kramida *et. al*, 2012), $v_{\rm GR} = 0.636\,{\rm km\,s^{-1}}$ is the solar gravitational redshift, and c is the speed of light. Then the core velocities of Hα measured within this study are offset only about $(\lambda_0 - \lambda_{\rm R})c/\lambda_0 = 0.5\,{\rm km\,s^{-1}}$ with respect to the local standard of rest at the target area, with the following consequences:

- the zero of $v_{\rm C}$ and all values of $v_{\rm BI}$ in Fig. 10 should be shifted redward (*i.e.*, up) about $0.5\,{\rm km\,s^{-1}}$,
- the zeros of the $v_{\rm C}$ axes in Figs. 11 and 12 should be shifted redward (*i.e.*, to the right) about $0.5\,{\rm km\,s^{-1}}$,
- most of the positive values of $v_{\rm C}$ indicated by the redshifts of the Hα core may represent the actual mass downflows.

7. Conclusions

A selected network element exhibits distinct spectral characteristics seen in their temporal evolutions and scatter plots correlating pairs of values from the same instant. In general, this involves:

- the fit width variations about $\pm 5\,\%$, *i.e.*, a few tens of milliångströms with respect to the average of 1.01 Å,
- the core intensity variations about $\pm 10\,\%$ with respect to the average,
- the core velocity variations from 0 to $4\,\mathrm{km\,s^{-1}}$ about the average of $1.5\,\mathrm{km\,s^{-1}}$, implying a redshift,
- the core asymmetry variations of the Hα line core up to $1\,\mathrm{km\,s^{-1}}$ about the average of $0.5\,\mathrm{km\,s^{-1}}$, suggesting an inverse-C bisector.

The Hα core width tends to correlate with the Dopplershift and anticorrelate with the asymmetry, suggesting that more redshifted Hα profiles are wider and the broadening of the Hα core is accompanied with a change of the core asymmetry from redward to blueward. We found also a striking anticorrelation between the core asymmetry and the Dopplershift, suggesting also a change of the core asymmetry from redward to blueward, with an increasing redshift of the Hα core. A question is which of these patterns are unique just for the network and which are also common in the internetwork. This can be resolved in a stand-alone study, comparing the spectral characteristics of the Hα line in the network and internetwork. Finally, an absence of blueshift and detected intensity and velocity variations probably exclude a presence of Alfvén waves in the selected network element according to the criteria given in Jess *et al.* (2009).

Acknowledgements. This work was supported by the Slovak Research and Development Agency under the contract No. APVV-0816-11. This work was supported by the Science Grant Agency - project VEGA 2/0108/12. This article was supported by the realization of the Project ITMS No. 26220120029, based on the supporting operational Research and development program financed from the European Regional Development Fund. The Technology Foundation STW in the Netherlands financially supported the development and construction of the DOT and follow-up technical developments. The DOT has been built by instrumentation groups of Utrecht University and Delft University (DEMO) and several firms with specialized tasks. The DOT is located at Observatorio del Roque de los Muchachos (ORM) of Instituto de Astrofísica de Canarias (IAC). DOT observations on 19 October 2005 have been funded by the OPTICON Trans-national Access Programme and by the ESMN-European Solar Magnetic Network - both programs of the EU FP6.

References

Alfvén, H.: 1947, *Mon. Not. R. Astron. Soc.* **107**, 211

Bettonvil, F.C.M., Hammerschlag, R.H., Sütterlin, P., Rutten, R.J., Jägers, A.P.L., Sliepen, G.: 2006, in *Society of Photo-Optical Instrumentation Engineers (SPIE) Conference Series*, eds.: Ian S. McLean and Masanori Iye, 6269, 12,

Erdélyi, R., Fedun, V.: 2007, *Science* **318**, 1572

Gaizauskas, V.: 1976, *JRASC* **70**, 1

Hammerschlag, R.H., Bettonvil, F.C.M.: 1998, *New A Rev.* **42**, 485

Heggland, L., Hansteen, V.H., De Pontieu, B., Carlsson, M.: 2011, *Astrophys. J.* **743**, 142

Jess, D.B., Mathioudakis, M., Erdélyi, R., Crockett, P.J., Keenan, F.P., Christian, D.J.: 2009, *Science* **323**, 1582

Keller, C.U., von der Lühe, O.: 1992, *Astron. Astrophys.* **261**, 321

Kontogiannis, I., Tsiropoula, G., Tziotziou, K.: 2010, *Astron. Astrophys.* **510**, A41

Koza, J., Sütterlin, P., Rybák, J., Hammerschlag, R.H., Gömöry, P., Kučera, A.: 2013, *Sol. Phys.* , submitted, Paper I

Kramida, A., Ralchenko, Yu., Reader, J., and NIST ASD Team: 2012, *NIST Atomic Spectra Database (ver. 5.0), [Online]. Available: http://physics.nist.gov/asd*, National Institute of Standards and Technology, Gaithersburg, MD

Leenaarts, J., Rutten, R.J., Sütterlin, P., Carlsson, M., Uitenbroek, H.: 2006, *Astron. Astrophys.* **449**, 1209

Leenaarts, J., Carlsson, M., Rouppe van der Voort, L.: 2012, *Astrophys. J.* **749**, 136

Mathioudakis, M., Jess, D.B., Erdélyi, R.: 2012, *Space Sci. Rev.*, Online First, 94

Neckel, H: 1999, *Sol. Phys.* **184**, 421

Osterbrock, D.E.: 1961, *Astrophys. J.* **134**, 347

Rutten, R.J., Hammerschlag, R.H., Bettonvil, F.C.M., Sütterlin, P., de Wijn, A.G.: 2004, *Astron. Astrophys.* **413**, 1183

Schoolman, S.A.: 1972, *Sol. Phys.* **22**, 344

Uitenbroek, H.: 2006, *Astrophys. J.* **639**, 516